

# Extended emission-line regions in low-redshift quasars: Dependence on nuclear spectral properties<sup>★</sup>

Bernd Husemann<sup>1</sup>, Lutz Wisotzki<sup>1</sup>, Sebastian F. Sánchez<sup>2</sup>, and Knud Jahnke<sup>3</sup>

<sup>1</sup> Astrophysikalisches Institut Potsdam, An der Sternwarte 16, 14482 Potsdam, Germany

<sup>2</sup> Centro Astronómico Hispano Alemán de Calar Alto (CSIC-MPIA), E-4004 Almería, Spain

<sup>3</sup> Max-Planck-Institut für Astronomie, Königsstuhl 17, D-69117 Heidelberg, Germany

## ABSTRACT

**Aims.** We searched for the presence of extended emission-line regions (EELRs) around low-redshift QSOs.

**Methods.** We observed a sample of 20 mainly radio-quiet low-redshift quasars ( $z < 0.3$ ) by means of integral field spectroscopy. After decomposing the extended and nuclear emission components, we constructed [O III]  $\lambda 5007$  narrow-band images of the EELR to measure the total flux. From the same data we obtained high S/N ( $> 50$ ) nuclear spectra to measure properties such as [O III]/H $\beta$  flux ratios, Fe II equivalent widths and H $\beta$  line widths.

**Results.** A significant fraction of the quasars (8/20) show a luminous EELR, with detected linear sizes of several kpc. Whether or not a QSO has a luminous EELR is strongly related with nuclear properties, in the sense that an EELR was detected in objects with low Fe II equivalent width and large H $\beta$  FWHM. The EELRs were detected preferentially in QSOs with larger black hole masses. There is no discernible relation, however, between EELR detection and QSO luminosity and Eddington ratio.

**Key words.** Galaxies: active - quasars: emission-lines - Galaxies: ISM

## 1. Introduction

Quasars may show extended emission-line regions (EELRs) stretching over characteristic scales of ten to hundred kpc. Luminous EELRs have been found in particular around steep-spectrum radio-loud quasars (RLQs, Boroson & Oke 1984; Heckman et al. 1991; Crawford & Vandervorst 2000; Stockton et al. 2002; Fu & Stockton 2006) and also radio galaxies (e.g. Villar-Martín et al. 2006, 2007). There are also indications that radio-quiet quasars (RQQs) can have EELRs (e.g., Boroson et al. 1985; Stockton & MacKenty 1987; Bennert et al. 2002). Most existing studies, however, are based either on long-slit spectroscopy or on narrow-band imaging; while the former technique will generally capture only part of any extended emission, the latter does not provide any spectroscopic information.

Integral field spectroscopy is a relatively new and powerful tool to study AGN host galaxies. The combined diagnostic power of imaging and spectroscopy allows for a flexible treatment of the data, facilitating the construction of broad- or narrow-band images, of 2-dimensional velocity maps as traced by emission or absorption lines, or the spectral analysis of selected regions within the field of view.

Here we present preliminary results from a study of 20 low-redshift QSOs, most of which are RQQs, observed with an integral field unit (IFU). After decomposing nuclear and extended emission we identified 8 quasars with clearly detectable EELRs. We focus on exploring the relation between the nuclear spectral properties of a QSO and the existence or non-existence of a luminous EELR. A full account of our IFU study will be given

in a separate paper (Husemann et al., in preparation; hereafter Paper II).

## 2. Observations and Data Reduction

We targeted a sample of 20 low-redshift ( $z < 0.3$ ) QSOs, selected from the Palomar-Green Survey (PG, Schmidt & Green 1983) and from the Hamburg/ESO Survey (HES; Wisotzki et al. (2000); Wisotzki et al., in prep.). The QSOs have apparent magnitudes in the range of  $V \sim 14 - 17$ ; corresponding to typical luminosities of  $M_V < -23$ . Three objects are steep-spectrum RLQs, another one is classified as a flat-spectrum RLQ; all the other sources are known to be radio-quiet. To our knowledge, this is the largest sample of bright quasars observed with an IFU so far.

We employed the Potsdam Multi-Aperture Spectrophotometer (PMAS; Roth et al. 2005), mounted on the 3.5 m telescope at Calar Alto Observatory, for two observing runs in September 2002 and in May 2003. The PMAS lens array was used at a spatial pixel ('spaxel') scale of  $0.5'' \times 0.5''$ , which for  $16 \times 16$  spaxels resulted in a field of view of  $8'' \times 8''$ . At the typical redshifts of our targets we were able to sample the quasar environment with a resolution of  $\sim 1$  kpc, and cover linear extents of up to  $\sim 20$  kpc in diameter.

All observations used the V300 grating to map the spectral features around the H $\alpha$  and H $\beta$  emission lines in a single setup. This yielded a moderate spectral resolution of approximately  $6.5 \text{ \AA}$  FWHM as measured by night sky emission lines. The total integration time for each object was 1–2 hours divided into several 30–45 min. exposures. Each individual exposure reaches a S/N level for the integrated nuclear quasar spectrum of already more than 50 per pixel in the continuum.

The raw data were homogeneously reduced using the PMAS reduction package *P3D* by Becker (2002). Due to substantial

Send offprint requests to: bhusemann@aip.de

<sup>★</sup> Based on observations collected at the Centro Astronómico Hispano Alemán (CAHA) at Calar Alto, operated jointly by the Max-Planck-Institut für Astronomie and the Instituto de Astrofísica de Andalucía (CSIC)

fibre-to-fibre variations in the wavelength calibration of more than  $0.7 \text{ \AA}$  rms, we used elements of the general reduction package *R3D* for fibre-fed IFUs (Sánchez 2006) to reduce this scatter to  $0.25 \text{ \AA}$  rms. We extracted and subsequently subtracted a mean sky spectrum from those spaxels in each science datacube that were deemed free of emission from the target itself. The data reduction will be described in full detail in Paper II.

### 3. Results

#### 3.1. Quasar-EELR decomposition

In order to measure the properties of EELRs, any possible contamination by the quasar nuclear emission had to be minimised. Three components are expected that need to be carefully deblended: Nuclear emission from the AGN point source; the stellar component of the host galaxy; and any possible resolved extended line emission. We found that in our luminous quasars, no significant evidence for a resolved stellar continuum above the noise could be found in our data, and we only needed to deblend the nuclear source and the extended line emission.

After running several tests we adopted the iterative decomposition method by Christensen et al. (2006). Briefly, a quasar spectrum is extracted from the spaxels at the position of the quasar, assuming that the contribution of the EELR and the stellar component is negligible for these spaxels. By dividing the spectrum of each spaxel by the quasar spectrum in the wavelength range bracketing a broad emission line (e.g.  $H\alpha$  or  $H\beta$ ), an appropriate scale factor is determined for each spaxel. A complete datacube of the quasar emission using the previously determined scale factors is then constructed. By subtracting the quasar datacube from the original one, a residual datacube containing any possible EELR is obtained. The process can be iterated by extracting a new quasar spectrum from the previous reconstructed quasar datacube; however, our solution converged already after the first iteration. This method showed the best results and minimal PSF subtraction artefacts compared to other strategies such as off-band image subtraction or PSF synthesis (Jahnke et al. 2004; Sánchez et al. 2004) that we also explored. However, the method is not perfect, and there are frequently some oversubtraction signatures at the quasar position (cf. Fig. 1). This happens because the extracted quasar spectrum contains a small fraction of the extended narrow emission line even if the scale factors were properly determined by the broad  $H\beta$  line.

For the present paper we focus on the narrow wavelength range containing the  $H\beta$  and the  $[\text{O III}]$  doublet  $\lambda\lambda 4959, 5007$ . The scale factor can therefore safely assumed to be a constant for each spectrum. Collapsing the residual data cube within  $\pm 20 \text{ \AA}$  centred on the nuclear  $[\text{O III}]$  peak wavelength, we could then produce narrow band  $[\text{O III}]$  images for each quasar. Figure 1 presents the results, displaying all 8 quasars with a detected EELR in  $[\text{O III}]$ . In the bottom row we also show the residuals for a representative subset of 3 (out of 12) undetected sources, to give the reader a visual impression of the significance of the detections.

#### 3.2. EELR fluxes

Examining the extracted  $[\text{O III}]$  narrow band images after subtraction of the quasar nuclei, we found that a significant fraction (8/20) of our objects contain a luminous EELR. We measured the total fluxes in these extended emission components by summation of all spaxels in the narrow band images, except those

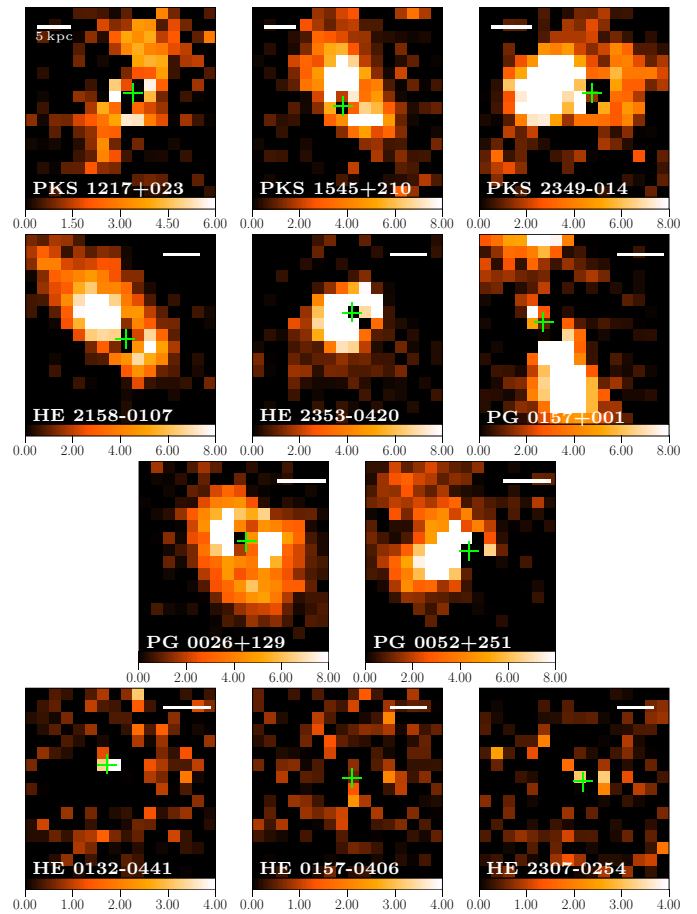


**Fig. 1.** Nucleus-subtracted  $[\text{O III}]$  narrow-band images extracted from the datacubes. All 8 quasars with clearly detected EELR are shown in the top three rows. The bottom row presents three example cases with non-detected EELR for comparison. In each panel, the position of the quasar is indicated by a green cross. Note that the apparent holes at most quasar locations are due to oversubtraction and thus not real (see text for details). The colour coded line flux is in units of  $10^{-16} \text{ erg/s/cm}^2/\text{arcsec}^2$ . All frames are  $8''$  on the side and oriented such that N is right and E is up. The white marker shows a 5kpc linear scale at the quasar redshift.

used to extract the quasar spectrum as these spaxels are slightly affected by oversubtraction of the quasar emission. In the case of PG 0157+001, the EELR is evidently larger than the PMAS field of view (see Fig. 1), and a significant fraction of the total flux may be missed by our data. We therefore treat the measured EELR flux for this object as a *lower limit*. In all other cases we find the EELRs to be reasonably well contained within the recorded images.

For the objects showing no sign of an EELR we could only estimate upper limits to fluxes. We simply adopted the extended flux from the faintest EELR measured in our sample as the upper limit for all those objects where there was no EELR detected. This is clearly a very conservative assumption which we plan to improve in the future by running dedicated simulations. The adopted limit was then scaled to the continuum flux density at  $5100 \text{ \AA}$  of each quasar continuum to account for the contrast between nuclear and extended emission.

Three of our QSOs were already imaged through narrow-band filters by Stockton & MacKenty (1987). Despite the different observing techniques, our  $[\text{O III}]$  EELR luminosities agree

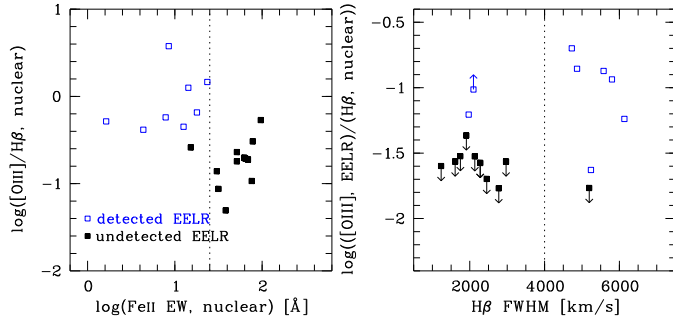


**Fig. 2.** Left panel: Nuclear [O III]/H $\beta$  flux ratio plotted against the nuclear Fe II equivalent width. QSOs with a detected EELR are denoted by the open squares, the undetected ones are shown as upper limits. The dashed line indicates a suggestive separation between the detected and non-detected EELRs. Right panel: Total EELR flux, normalised to the nuclear H $\beta$  flux, plotted against the FWHM of the broad H $\beta$  component. Note the *lower* limit for PG 0157+001 for which the EELR is larger than our field of view.

within a factor of  $\sim 2$ – $3$  with their measurements. Three QSOs were furthermore contained in the narrow-band HST study by Bennert et al. (2002), which however revealed mainly high-surface brightness features less than  $1''$  to the QSO nuclei.

In order to obtain a measure of EELR strength independent of the spectro-photometric calibration, Galactic foreground extinction and scaling with quasar luminosity, we divided the EELR fluxes (and upper limits) by the fluxes in the broad H $\beta$  components of the individual quasars.

### 3.3. Spectral properties of the quasars

As mentioned above, each datacube provided us also with a high S/N spectrum of the central quasar over essentially the full optical wavelength range, albeit at moderate spectral resolution. We extracted the nuclear emission line properties by fitting a superposition of simple analytical functions to the line profiles, using the Levenberg-Marquardt  $\chi^2$  minimisation algorithm. For our narrow wavelength range, a straight line was sufficient to model the local continuum of each spectrum. The broad Balmer lines were modelled with two or three independent Gaussian components, in accordance with previous experiences by several others (e.g. Sulentic et al. 2002; Véron-Cetty et al. 2006). We fitted the [O III]  $\lambda\lambda 4959, 5007$  doublet as a system of two Gaussians with the same line width, fixed rest-frame wavelength separation and a fixed line ratio of 1:3.

Both H $\beta$  and the [O III] doublet can be heavily affected by Fe II emission line complexes. The most prominent is the Fe II  $\lambda\lambda 4924, 5018$  doublet, which we modelled similarly to the [O III] doublet, but with a fixed line ratio of 1.28 ( $\lambda 5018/\lambda 4924$ ). We also used the Fe II complex ( $5100\text{Å}$ – $5405\text{Å}$ ) longwards of [O III] to measure the strength of the Fe II emission in those cases where the Fe II emission is weak. A linear quasi-continuum was estimated from the bracketing emission-line free regions and subtracted from the quasar spectrum. We integrated the residual flux in the given wavelength interval to estimate the Fe II flux and equivalent widths.

### 3.4. Black hole masses and accretion rates

We estimated black hole masses ( $M_{\text{BH}}$ ) for all objects from our single epoch quasar spectra, using the virial method

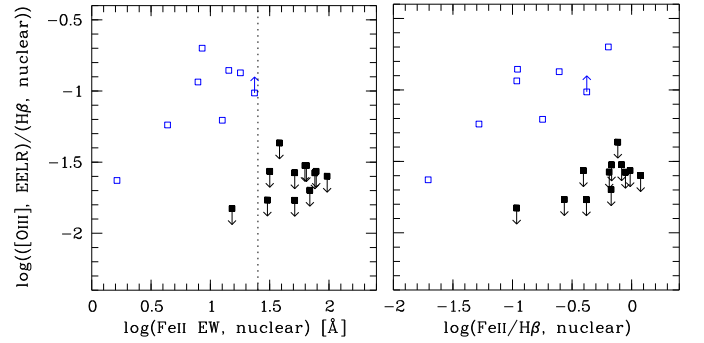


**Fig. 3.** Comparison of the extended [O III] flux (again normalised to nuclear H $\beta$ ) with two different measures of Fe II strength. Left: Equivalent width of the Fe II emission; right: Fe II flux divided by the broad H $\beta$  flux. Symbols as in Fig. 2.

(Vestergaard & Peterson 2006). The method assumes that the broad line region (BLR) clouds are in gravitational equilibrium within the black hole potential, so that the central mass can be estimated as  $M_{\text{BH}} = fRv^2/G$  where  $f$  is a geometry-dependent factor that needs to be calibrated empirically. The radius  $R$  of the BLR can be predicted from the quasar luminosity using the radius-luminosity scaling relation  $R \propto L^{0.5}$  (Bentz et al. 2006). The characteristic velocity of the emitting clouds can be estimated in two ways, from the FWHM of broad emission lines or from the emission line dispersion  $\sigma$ . Collin et al. (2006) showed recently that the  $M_{\text{BH}}$  estimates are sensitive to the line profile shape and argued that  $\sigma_{\text{line}}$  gives more robust  $M_{\text{BH}}$  estimates than those based on  $\text{FWHM}_{\text{line}}$ . We compared both velocity measures and found that while the differences were non-negligible, they are not important for the purpose of the present paper. We therefore adopted the H $\beta$  line FWHM together with the scaling relation by Vestergaard & Peterson (2006) to obtain black hole masses.

Having obtained black hole masses, we could also estimate the ‘Eddington ratios’ of each quasar, i.e. the actual accretion rates divided by the Eddington rates, or in terms of observables, the bolometric luminosities divided by the luminosities that each object would have if radiating at the Eddington limit,  $L_{\text{bol}}/L_{\text{Edd}}$ . We adopted a canonic bolometric correction (e.g., Kaspi et al. 2000) of  $L_{\text{bol}} = 9\lambda L_{\lambda}(5100\text{Å})$ .

## 4. Discussion

### 4.1. Relations between EELR detection and nuclear spectral properties

In essentially all quasars where we detected extended emission in [O III], we also see a significant nuclear [O III] component. We also measured Fe II emission to be very weak. This is shown in the left panel of Fig. 2, where we plot the *nuclear* [O III]/H $\beta$  flux ratio against the Fe II equivalent width. Apparently, quasars with and without an EELR populate two distinct regions on this plot. By drawing a vertical line at log(Fe II EW) = 1.4, the two groups are well separated except for a single interloper with undetected EELR, which might be due to relatively poor observing condition for that objects (seeing  $\sim 1.8''$ ). Figure 3 compares two different measures of relative Fe II strength with the H $\beta$  normalised flux ratio. In the left panel we employ the Fe II EW as used already in Fig. 2, and in the right panel we show the Fe II/H $\beta$  ratio. While the objects with and without detected EELR are

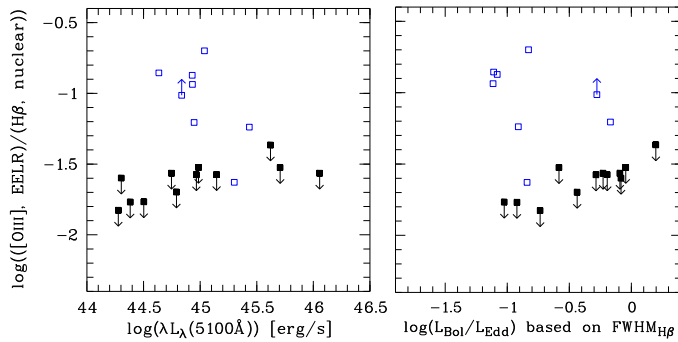


**Fig. 4.** The EELR flux normalised by the nuclear  $H\beta$  flux plotted against continuum luminosity at  $5100\text{ \AA}$  (left), and against Eddington ratios (right). Symbols as in Fig. 2.

again clearly separated in the former diagram, the distribution of  $\text{Fe II}/H\beta$  values is essentially identical for the two groups.

Comparing the normalised EELR flux with the FWHM of the broad  $H\beta$  emission line we find an even clearer separation, albeit with a slightly larger number of interlopers. This is shown in the right-hand panel of Fig. 2, where 6/8 of all objects with a detected EELR have line widths well in excess of  $\text{FWHM}(H\beta) \sim 4000\text{ km/s}$ . On the other hand, all quasars (except one) with non-detected EELR have  $1000\text{ km/s} \lesssim \text{FWHM}(H\beta) \lesssim 3000\text{ km/s}$ . We note that the one exception, the RQQ PG 2214+139 with  $\text{FWHM}(H\beta) \sim 5000\text{ km/s}$  and no detected EELR, shows a very peculiar multicomponent  $H\beta$  line shape. The two interlopers with  $\text{FWHM}(H\beta) < 4000\text{ km/s}$  have the largest  $\text{Fe II}$  EWs values among the objects with detected EELR.

#### 4.2. Luminosities, black hole masses and Eddington ratios

We now explore whether the above results can be related to more fundamental quantities such as luminosities, black hole masses and Eddington ratios. Figure 4 presents, in a similar way as in Fig. 3, the EELR flux normalised by the nuclear  $H\beta$  flux plotted against the continuum luminosity (left panel) and against the Eddington ratio (right panel). All objects have broadly similar continuum luminosities, which basically *rules out* the possibility that it is simply the luminosity of the quasar determining the EELR properties. The FWHM is then the dominant term in the computation of  $M_{\text{BH}}$ , so that a pattern very similar to that seen in  $\text{FWHM}(H\beta)$  arises also for  $M_{\text{BH}}$ . We find that a dividing line at  $\log(M_{\text{BH}}/M_{\odot}) = 8.5$  separates the objects having smaller black hole masses and non-detected EELRs from the objects with larger masses and detected EELRs. If on the other hand we consider the Eddington ratios, there is again *no* clear separation between the two groups, with the distribution of  $\log(L_{\text{bol}}/L_{\text{Edd}})$  covering the same range for detected and non-detected QSOs. We reiterate that this fact is independent of our choice of how to estimate black hole masses (Sect. 3.4).

## 5. Conclusions

By means of integral field spectroscopy, we have revealed the presence of extended emission line regions (EELRs) in a sample of predominantly radio-quiet low-redshift QSOs. The sizes and luminosities are much higher than those of the well-known EELRs in Seyfert galaxies, extending out to several kpc and therefore stretching over the entire host galaxy (and possibly beyond). Some 40 % of the objects in our sample show a prominent EELR, while we failed to detect any EELR signature in the re-

maining 60 %. The detection or non-detection of an EELR can be linked to the *nuclear* spectral properties of the quasar itself, independent of their radio classification, in excellent agreement with what Boroson & Oke (1984) and Boroson et al. (1985) found from their off-nuclear long-slit spectra. Our observations go further in that our integral field spectral data map out the entire nuclear-subtracted EELRs and derive their luminosities.

Correlations between various nuclear spectral properties were already studied by many authors (e.g. Boroson & Green 1992; Sulentic et al. 2000; Netzer et al. 2004). Here we provide new evidence that properties of the nuclear spectra, depending on the sub-pc scale conditions in AGN, are linked to properties of the host galaxies extending over several kpc. It thus appears possible to predict with high confidence whether or not a QSO will show a very extended emission line region just from its nuclear spectrum: If it has broad  $H\beta$  and weak  $\text{Fe II}$ , it will probably have not only strong nuclear, but also strong extended  $[\text{O III}]$  emission.

It is tempting to interpret this relation between sub-pc and super-kpc scales in the context of the current discussion about AGN feedback affecting the host galaxies. Since we can rule out the QSO luminosity as a main driver of the differences between presence or absence of an EELR, the remaining possibilities are that there could be differences in the structure of the nuclear region (obscuration in connection with possible inclination effects); or differences due to an outflow or jet, or the host galaxies of the two QSO classes are intrinsically different, in particular with respect to their overall distribution of warm ionised gas. We conclude that QSO host galaxies come in at least two flavours: with or without extended ionized gas. Whether this highlights different initial conditions or a sequence of evolutionary stages we cannot say at present. More and better quality data will be needed to elucidate these intriguing trends.

**Acknowledgements.** BH and LW acknowledge financial support by the DFG Priority Program 1177, grant Wi 1369/22-1. KJ acknowledges support through the DFG Emmy Noether-Program.

## References

- Becker, T. 2002, PhD thesis, (University of Potsdam)
- Bennert, N., Falcke, H., Schulz, H., Wilson, A. S., & Wills, B. J. 2002, *ApJ*, 574, L105
- Bentz, M. C., Peterson, B. M., Pogge, R. W., Vestergaard, M., & Onken, C. A. 2006, *ApJ*, 644, 133
- Boroson, T. A. & Green, R. F. 1992, *ApJS*, 80, 109
- Boroson, T. A. & Oke, J. B. 1984, *ApJ*, 281, 535
- Boroson, T. A., Persson, S. E., & Oke, J. B. 1985, *ApJ*, 293, 120
- Christensen, L., Jahnke, K., Wisotzki, L., & Sánchez, S. F. 2006, *A&A*, 459, 717
- Collin, S., Kawaguchi, T., Peterson, B. M., & Vestergaard, M. 2006, *A&A*, 456, 75
- Crawford, C. S. & Vanderriest, C. 2000, *MNRAS*, 315, 433
- Fu, H. & Stockton, A. 2006, *ApJ*, 650, 80
- Heckman, T. M., Lehnert, M. D., Miley, G. K., & van Breugel, W. 1991, *ApJ*, 381, 373
- Jahnke, K., Wisotzki, L., Sánchez, S. F., et al. 2004, *AN*, 325, 128
- Kaspi, S., Smith, P. S., Netzer, H., et al. 2000, *ApJ*, 533, 631
- Netzer, H., Shemmer, O., Maiolino, R., et al. 2004, *ApJ*, 614, 558
- Roth, M. M., Kelz, A., Fechner, T., et al. 2005, *PASP*, 117, 620
- Sánchez, S. F. 2006, *Astronomische Nachrichten*, 327, 850
- Sánchez, S. F., García-Lorenzo, B., Mediavilla, E., González-Serrano, J. I., & Christensen, L. 2004, *ApJ*, 615, 156
- Schmidt, M. & Green, R. F. 1983, *ApJ*, 269, 352
- Stockton, A. & MacKenty, J. W. 1987, *ApJ*, 316, 584
- Stockton, A., MacKenty, J. W., Hu, E. M., & Kim, T.-S. 2002, *ApJ*, 572, 735
- Sulentic, J. W., Marziani, P., Zamanov, R., et al. 2002, *ApJ*, 566, L71
- Sulentic, J. W., Zwitter, T., Marziani, P., & Dultzin-Hacyan, D. 2000, *ApJ*, 536, L5
- Véron-Cetty, M.-P., Joly, M., Véron, P., et al. 2006, *A&A*, 451, 851
- Vestergaard, M. & Peterson, B. M. 2006, *ApJ*, 641, 689

Villar-Martín, M., Sánchez, S. F., De Breuck, C., et al. 2006, *MNRAS*, 366, L1  
 Villar-Martín, M., Sánchez, S. F., Humphrey, A., et al. 2007, *MNRAS*, 378, 416  
 Wisotzki, L., Christlieb, N., Bade, N., et al. 2000, *A&A*, 358, 77

## List of Objects

‘PG 0157+001’ on page 2

‘PG 2214+139’ on page 4